



Enhancement of electrical and magnetic properties in acceptor-doped BaTiO₃ ferroelectric ceramics

K. Madhan¹ · C. Jagadeeshwaran¹ · R. Murugaraj¹

Received: 15 September 2018 / Accepted: 14 December 2018 / Published online: 2 January 2019
© Springer Science+Business Media, LLC, part of Springer Nature 2019

Abstract

BaTi_{1-x}Mn_xO₃ ($x = 0.00, 0.25, 0.50, 0.75$ mol%) (BTMO) ceramics were synthesized through sol–gel combustion method. The structural studies suggested that Mn-doped BaTiO₃ (BTO) ceramics exhibit a tetragonal structure with $P4mm$ space group via Rietveld refinement analysis. Also, the phonon mode at 308 cm⁻¹ through Raman spectral analysis confirms the local structure of tetragonal symmetries. The redshift observed in UV-absorption spectra indicates a decrease of optical band gap from 3.13 to 2.71 eV with increasing Mn²⁺ doping. The observed decrease in the intensity of PL emission spectra was due to an increase of Mn²⁺ concentration. This indicates that a decrease in oxygen vacancies and a reduction in the number of electrons attributed to the Burstein–Moss shift. The carrier hopping process between Mn²⁺ and Mn³⁺ is responsible for dielectric as well as magnetization behavior. The ferroelectric double hysteresis loops are related to a ferroelectric and anti-ferroelectric order and it increases with the increase of Mn ion concentration in BTO. Through P–E measurements, the value of remnant electric polarization and coercive field found to be increased with Mn concentration in BTO samples. For BTO sample, two EPR signals with $g = 1.969$ and $g = 2.000$ singlets can be assigned with ionized Ba and Ti-vacancy defects. In addition, the EPR signal for BTMO shows a good correlation with Ti vacancies as compensating for lattice defects. Further, the Mn doping induced a weak ferromagnetic to ferromagnetic state due to free carrier concentrations.

1 Introduction

In perovskite (ABO₃) type oxides, BTO ceramics is one of the most interesting ferroelectric materials due to its intricate physical properties. It is widely investigated by researcher due to the usage of BTO in multilayer ceramic capacitors (MLCC), ferroelectric random access memories (Fe-RAM) and its extensive applications in piezoelectric actuators, pyroelectric detectors, electro-optical systems, electrochemical systems, and positive temperature coefficient devices [1–5]. The crystalline phase of BTO at room temperature is tetragonal and it transforms to the cubic structure above Curie temperature of $T_c \sim 130$ °C. It also exists in the orthorhombic phase at 0 °C and rhombohedral phases at below -90 °C and at above 1460 °C it exists in hexagonal phase [1]. In order to enhance the ferroelectric properties of BTO, many researchers have been extensively studied through the effects of doping with various oxides, such

as Bismuth, Lanthanum, and Yttrium, to tailor the defect structure [6, 7]. In particular, it has been found that the doping of manganese (Mn) ions is effective to improve the microstructural, optical and electrical properties of BaTiO₃. Although, the Mn doping in BTO depress the grain size and enhances the electrical resistivity as like the donor-doped positive temperature coefficient of resistance (PTCR) near the Curie temperature of BTO [6]. On the other hand, the doping of Mn ion at Ti ion site as an acceptor-type doping will produce oxygen vacancies at O²⁻ sites to maintain charge neutrality [8]. In the literature, several methods were employed to prepare BTO and Mn-doped BTO such as solid state reaction, hydrothermal synthesis, and thin film technology [9–14]. In particular, the sol–gel technique can be considered as a most influential technique for the preparation of the BTO and Mn-doped BTO samples. Because, this method is low-temperature processing, good chemical homogeneity, non-vacuum requirement, the smaller crystallite size of the synthesized compounds, and in addition to less equipment and potentially less expensive [15]. Still, the doping of Mn ion has been hardly reported to exhibit good photoluminescence properties of perovskite compounds [11]. Maneeshya et al. has suggested that the broad photoluminescence band

✉ R. Murugaraj
r.murugaraj@gmail.com

¹ Department of Physics, MIT Campus, Anna University, Chennai 600044, India

is usually observed at low temperature and this behavior is associated with the presence of lattice imperfections, vacancies or defects in the doped BTO lattices [15]. In addition, the electron paramagnetic resonance (EPR) technique is also used as a powerful tool for identifying the site occupation of Mn ion at the Ti site (through defects formations). Da-Yong Lu et al. has observed two EPR signals for Mn-doped BTO samples with $g = 1.974$ and 2.004 and clarified with Ba vacancy and Ti vacancy defects [16]. However, the Mn-doped BTO ferroelectric system exhibits an abnormal double ferroelectric hysteresis (P–E) loop in ferroelectric (FE) state due to aging and also, a good number of studies have been reported in the literature on FE aging behavior [6–8]. The observed double hysteresis phenomena are associated with the reversible domain switching which is driven by the symmetry conforming properties of oxygen vacancies [17]. However, there are limited reports available on the optical and multifunctional behavior of the Mn-doped BTO ceramics.

On the other hand, the present work on Mn^{2+} doped BTO at very low concentration using sol–gel combustion method has not been performed to the best of our knowledge. Hence an effort has been made to enhance the optical, electrical and magnetic properties. Interestingly, we have observed the simultaneous enhancement of weakferromagnetic (WFM) to ferromagnetic (FM) phase transition and high dielectric constant due to Mn^{2+} doping. Further, the carrier hopping process between Mn^{2+} and Mn^{3+} is also responsible for observed dielectric as well as magnetization nature.

2 Experimental details

Mn-doped BTO system $\text{BaTi}_{1-x}\text{Mn}_x\text{O}_3$ ($x = 0.0, 0.25, 0.50, 0.75$ mol%) were synthesized by sol–gel combustion method. High purity analytical grade Barium nitrate ($\text{Ba}(\text{NO}_3)_2$), Titanium isopropoxide ($\text{C}_{12}\text{H}_{28}\text{O}_4\text{Ti}$), Manganese acetate ($\text{Mn}(\text{CH}_3\text{COO})_2$), citric acid ($\text{C}_6\text{H}_8\text{O}_7$), polyethylene glycol (PEG-400), ammonia (NH_4OH), acetic acid (CH_3COOH) and ethanol ($\text{C}_2\text{H}_6\text{O}$) were employed as raw materials. Firstly, the specific amount of titanium isopropoxide was dissolved in 1:1 ratio of acetic acid and ethanol solution. Then the required amount of distilled water was added slowly with constant stirring to get a homogeneous solution. The PEG in 1:2 molar ratio with respect to the metal cations was added to the solution. After that citric acid in 2:1 molar ratio with respect to the sum of metal cations was added to the solution as a fuel as well as a chelator. The PH value of ~ 9 was maintained by adding the required liquid ammonia solution. Finally, the manganese acetate and barium nitrate solution were added under constant stirring at 80°C for 4 h to form a wet gel. Thereafter, the dried gel was formed through the combustion process. The dried samples

were grounded in an agate mortar and pestle till fine powder of $\text{BaTi}_{1-x}\text{Mn}_x\text{O}_3$ was obtained. Then the calcination of Mn-doped BTO samples was carried out at 900°C for 3 h using the programmer controlled high-temperature furnace at a heating and cooling rate 5°C min^{-1} .

2.1 Characterization

The X-ray diffraction (XRD) pattern was measured using Bruker-D2 phaser diffractometer with $\text{Cu-K}\alpha$ ($\lambda = 1.5418 \text{ \AA}$) radiation with 0.02° scan step size from $(2\theta) 10^\circ$ – 80° at room temperature to confirm the phase purity of the synthesized samples. To determine the crystal structure, the Rietveld refinement method used for profile fitting of the XRD patterns, and by GSAS and EXPUGI packages [18]. Raman spectra of the prepared samples were measured using a micro-Raman spectrometer (LABRAM-HR) with 488 nm excitation using Ar^+ laser source and spot size of $2 \mu\text{m}$ using a $50\times$ objective lens. High-Resolution Scanning Electron Microscope (HRSEM) images of the prepared samples were recorded using Quanta 200 FEG scanning electron microscope with highly versatile with low vacuum (LV). Their solution is 1.2 nm gold particle separation on a carbon substrate was used to characterize the surface morphology of the sintered powder samples and grain size distributions were calculated using image software. The room temperature UV–Vis spectrometer (Shimadzu UV 2450 PC Spectrophotometer) and the energy band gap was estimated using *tauc* plot. The photoluminescence (Varian Cary Eclipse) measurements were carried out by fluorescence spectrometer with an excitation source of 435 nm. In this work, PL and Raman spectra peaks were fitted with Gaussian function independently and individual peaks were obtained through the deconvolution process using the Fityk software [19]. The EPR spectra were measured at room temperature using a JEOL model JES FA200 spectrometer with the measurement at X band frequency (8.75–9.65 GHz). The frequency dependent dielectric measurements were carried out on the sintered pellets by employing PSM1735NumetriQ, impedance meter. The room temperature polarization versus applied electric field (P–E) hysteresis behavior of BTMO samples was measured using a P–E loop tracer (Radiant Technologies) at different voltages a constant frequency of 20 Hz.

3 Results and discussion

3.1 Phase analysis

XRD pattern of pure and Mn-doped BTO samples synthesized by sol–gel combustion method and sintered at 900°C was shown in Fig. 1. The XRD pattern confirms the tetragonal perovskite structure with a space group $P4mm$ of all the samples

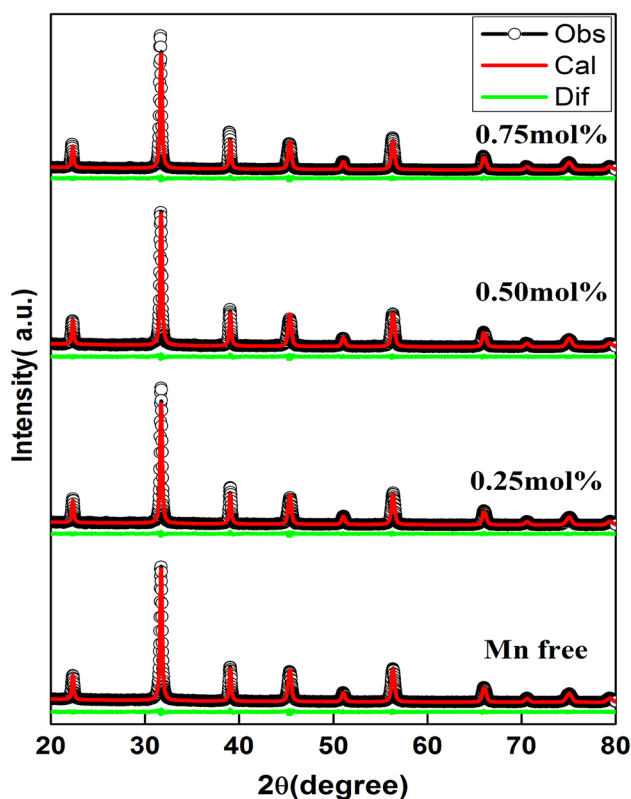


Fig. 1 XRD Rietveld refinement of a $\text{BaTi}_{1-x}\text{Mn}_x\text{O}_3$ ($x=0.00, 0.25, 0.50, 0.75$ mol%) samples

and no other impurity phases were observed. The sharp diffraction peaks confirm the formation of high purity and well crystalline BTMO samples. The structures of all the prepared samples were initially fitted with XRDA software using standard pattern of JCPDS card No. 79-2263. The average crystallite size was calculated using the Scherrer formula,

$$D = \frac{0.9\lambda}{\beta \cos \theta} \quad (1)$$

Table 1 XRD Rietveld refinement factors and tetragonal composition of $\text{BaTi}_{1-x}\text{Mn}_x\text{O}_3$ ($x=0.00, 0.25, 0.50, 0.75$ mol%) samples

Sample	BaTiO_3	$\text{BaMn}_{0.0025}\text{Ti}_{0.9975}\text{O}_3$	$\text{BaMn}_{0.005}\text{Ti}_{0.995}\text{O}_3$	$\text{BaMn}_{0.0075}\text{Ti}_{0.9925}\text{O}_3$
Crystallite size (nm)	34	43	46	49
Lattice strain (10^{-3})	3.52	2.76	2.60	2.48
X-ray density (gm/cm^3)	7.804	5.917	5.662	5.604
Lattice parameters				
a (Å)	4.0036	3.9982	4.0035	4.0055
c (Å)	4.0199	4.0169	4.0222	4.0247
c/a	1.0040	1.0046	1.0046	1.0047
Cell volume (Å^3)	64.435	64.214	64.471	64.576
R-factor (%)				
R_p	4.01	4.61	5.01	3.70
R_{wp}	5.20	6.12	6.68	4.98
χ^2	1.48	1.98	2.37	1.33

where D is the average crystallite size, λ is the wavelength of Cu $K\alpha$ line, β is the full width at half maximum (FWHM) and θ is the Bragg's diffraction angle. In addition, the XRD patterns were indexed with powder X software. The phase formation of BTMO samples is also dependent on the calcinations as well as the sintering temperature. The ionic radii of Mn ions are near to that of Ti^{4+} ion (0.605 Å) and smaller than that of the Ba ion (1.35 Å). Therefore, it is reasonable to imply that the Mn ion (0.46 Å) into doping of Ti sites of BTO lattice [9]. The average crystallite size of the samples increases as the content of Mn increases in the Ba-Ti-O lattice (34 nm to 49 nm). This may be due to the Mn ions involves in growth mechanism and hence increases the crystallite size of Mn-doped of BTO samples. The XRD data were further analyzed by Rietveld refinement using General Structural Analysis System (GSAS) program [18]. The obtained refinement parameters such as residual factor (R_{wp} , R_p , and χ^2), lattice parameters and unit cell volume were listed in Table 1. From Table 1, there is an increase in lattice constant and cell volume as the content of Mn increasing BTMO samples. The expansion in cell volume was observed in Mn-doped samples confirms that the transition metal ion (Mn) is being successfully incorporated into the host crystal lattice. As the content of Mn ion increases, there were slight increases in the lattice constant " a " and " c ", cell volume. It was observed that lattice strain, X-ray diffraction density will be gradual decreases and tetragonality (c/a) is slight increases [9]. This variation in lattice constant with Mn doping indicates the lattice distortion in BTMO samples.

3.2 Raman spectra analysis

Raman spectroscopy is a sensitive tool to detect subtle variation in the structure of small crystalline region below 2–3 nm within a much shorter duration (<1 ns). It is well known that XRD measurements and their analysis can clarify the average and static symmetries, whereas the Raman

scattering spectra can clarify the local and dynamic symmetries in the crystalline system. For that reason, Raman spectra were recorded on the pure and Mn-doped BTO samples and the observed results were shown in Fig. 2. In order to confirm the phase structure, in addition to XRD analysis, the Raman spectra were employed to emphasize the evidence of phase transitions. The tetragonal BTO contains 15 vibrational modes, including 12 optical modes, which can be represented as $\Gamma_{\text{opt}}=3A_1+B_1+4E$, where A_1 (longitudinal-optical) and E (transverse-optical). From these analysis, two asymmetric, broad and intense bands associated with A_1 (TO_2), A_1 (TO_3) optical modes, a weak band [A_1 (LO_3) + E (LO_3)] and [A_1 + E ($\text{TO} + \text{LO}$)] soft mode split from F_{1u} mode in cubic BTO, which contributed to a ferroelectricity in tetragonal BTO [20].

For the present BTMO samples, the peak intensity, full-width half maxima, and Raman bands were calculated from the measured Raman spectra and reported in Table 2. From Fig. 2, it is observed that the peak near to 248 cm^{-1} could

be associated with [$A_1(\text{TO})$] mode, sharp bands at approximately 306 cm^{-1} could be assigned to [$B_1, E(\text{TO} + \text{LO})$] modes, peak near 512 cm^{-1} was related to [$A_1, E(\text{TO})$] modes and at 717 cm^{-1} could be ascribed to [$A_1, E(\text{LO})$] modes. The Raman band peaks at 248 cm^{-1} and 512 cm^{-1} is attributed to broken translation symmetry due to the boundaries, defects or by possible short-range polar order regions existing in the tetragonal phase [21].

A high-intensity peak observed near 306 cm^{-1} for all the samples, which is more dominant and high sharpness, associated with the indication of the tetragonal phase. It can be concluded that the tetragonal phase might be determined by observing the relative intensity of the bands at and around 306 cm^{-1} . Further, the peak positioned at 109 cm^{-1} in the spectra correspond to the same symmetry of TiO_2 . The observed anti-resonance effect at 181 cm^{-1} suggests that the coexistence of coupling of TO modes associated with the tetragonal phase. However, the weak band at 639 cm^{-1} is not belonging to the tetragonal phase and it is associated with

Fig. 2 Raman spectra of a $\text{BaTi}_{1-x}\text{Mn}_x\text{O}_3$ ($x=0.00, 0.25, 0.50, 0.75$ mol%) samples

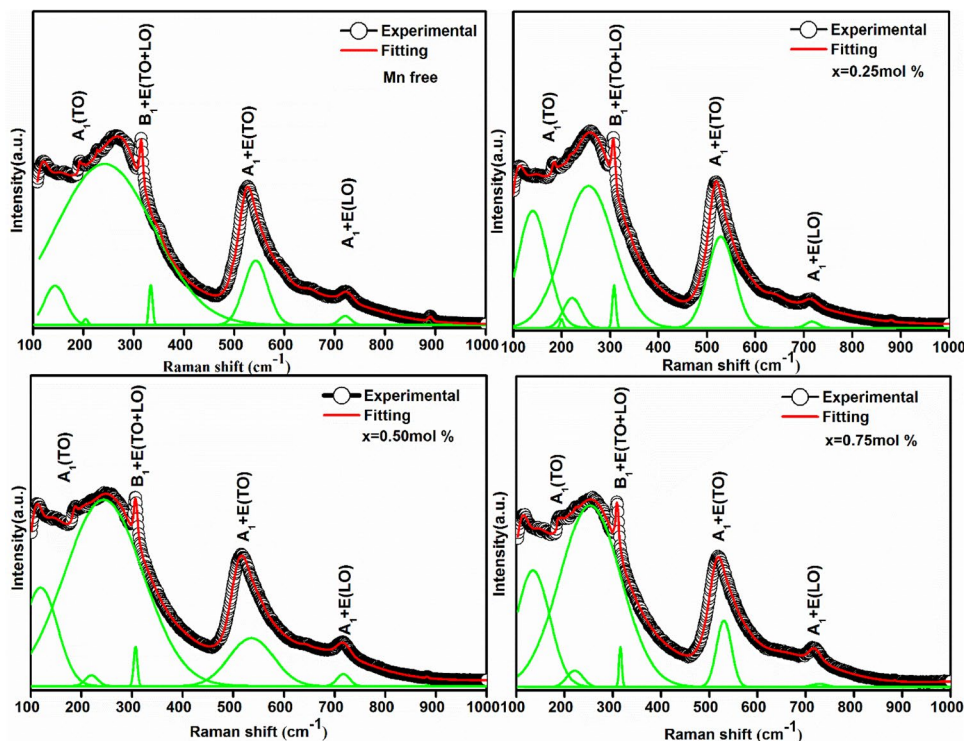


Table 2 Raman modes and full width half maxima of $\text{BaTi}_{1-x}\text{Mn}_x\text{O}_3$ ($x=0.00, 0.25, 0.50, 0.75$ mol%) samples

Raman modes	Wavenumber (cm^{-1})				FWHM (cm^{-1})			
	$x=0.0\%$	$x=0.25\%$	$x=0.50\%$	$x=0.75\%$	$x=0.0\%$	$x=0.25\%$	$x=0.5\%$	$x=0.75\%$
$[A_1(\text{TO})]$	248	255	273	253	182.48	121.96	79.25	151.80
$[B_1, E(\text{TO} + \text{LO})]$	306	307	307	308	9.00	8.2441	7.75	6.96
$[A_1, E(\text{TO})]$	512	529	516	515	38.39	65.989	32.73	37.89
$[A_1, E(\text{LO})]$	717	717	717	718	29.60	31.368	28.21	28.53

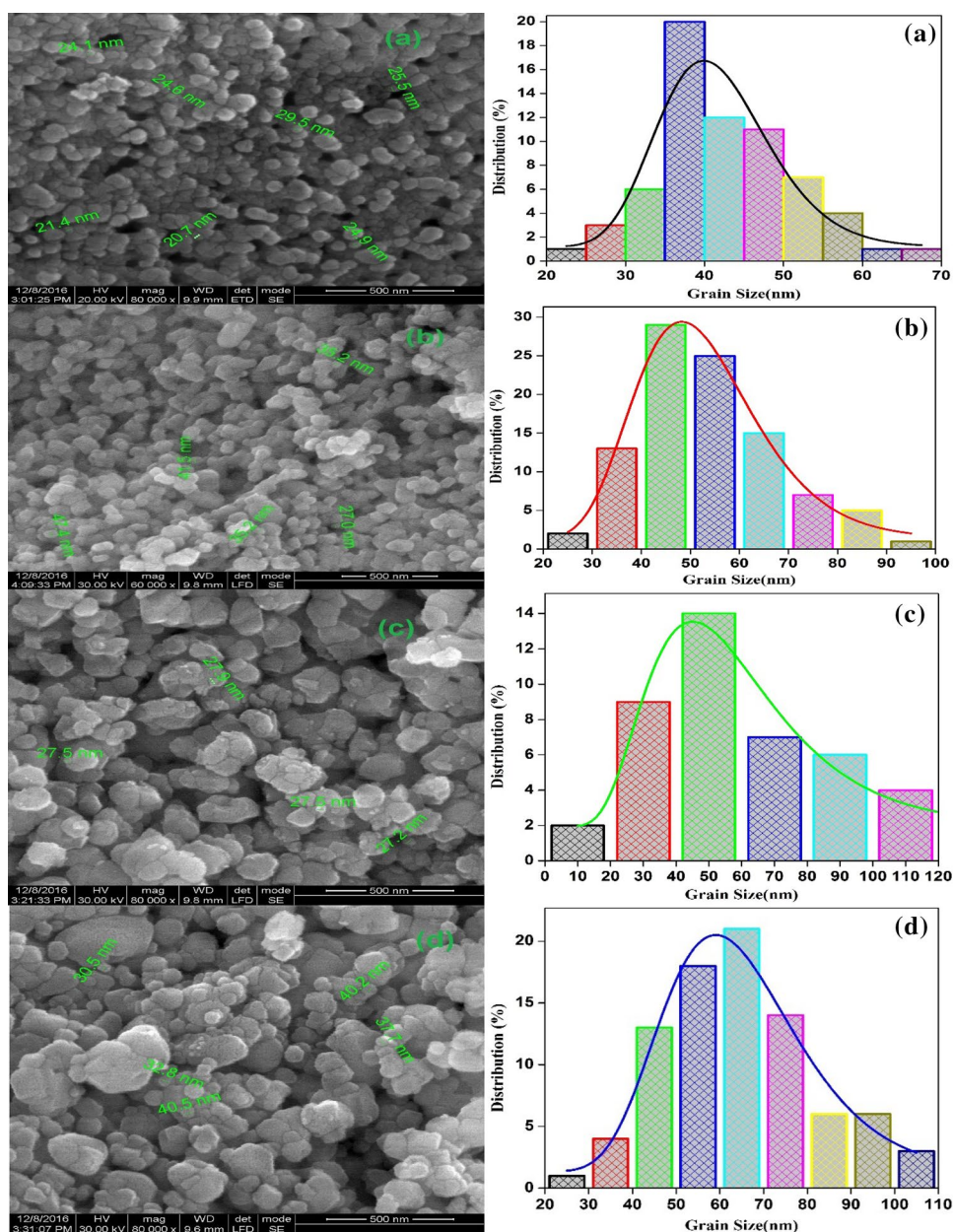
high-temperature perovskite phases of the BaO–TiO₂ system [21–23]. Especially, the small feature band at 882 cm⁻¹ may be attributed to the internal lattice defects or vacancies in BTO ceramic materials [22], while it does not observe in Mn-doped BTO ceramics. Therefore, this mode can be attributed to an internal deformation of the BO₆ octahedron caused by the charge difference of BTO samples [18].

3.3 Microstructure analysis

The SEM micrographs with a histogram of particle size distributions of all prepared BTO and BTMO samples were depicted in Fig. 3. It can be seen that all the samples composed of random and spherical-type nanoparticles

with relatively dense microstructure. The calculated average particle size and distribution was determined by *Image J* program [24]. It was observed that all the grains are agglomerated and smaller grains coalesce to the larger grains of increasing Mn doping concentration up to 0.75 mol%. Thus, the dopant concentration (Mn) influences the size of particles. The estimated grain size for pristine samples was around 41 nm as the Mn concentration increases, the grain size was increased to 63 nm are shown in Table 5. These results are inconsistent with crystallite size calculated from XRD data analysis. Hence, from the SEM micrograph, it could be concluded that grains observed by SEM consist of fine crystallites. Additionally, an insignificant difference in the form of

Fig. 3 HRSEM image and particle size distribution histogram of BaTi_{1-x}Mn_xO₃ (x = 0.00, 0.25, 0.50, 0.75 mol%) samples



agglomeration, size, and microstructure of the crystals was found among the pure and Mn-doped BTO samples [3, 25].

3.4 UV-absorption properties

UV-spectroscopy is commonly used to evaluate the optical absorption property of the semiconducting materials. Figure 4a shows the UV-spectra of the BTMO samples synthesized by a sol–gel combustion process. All the spectra exhibit the optical absorption edge located near 362 nm. The optical band gap energy was calculated by *tauc* plot and are shown in Fig. 4b. The absorption coefficient α and optical band gap E_g are related by this formula,

$$\alpha h\nu = (h\nu - E_g)^n \quad (2)$$

where h is Planck's constant, ν is frequency of incident radiation, $n = 1/2$ for the direct band and $n = 2$ for indirect band-gap semiconductor materials. The magnitude of the energy band gap is obtained through the interception of the straight line fitted to the low energy side of the curve. Literature review shows that the BTO is the direct band semiconductor materials [22]. The energy band gap values of pristine and Mn doping concentration at 0.25 mol%, 0.50 mol% and 0.75 mol% samples are 3.13 eV, 2.93 eV, 2.83 eV, 2.71 eV respectively. This indicates that the band gap E_g decreases gradually with the increase of Mn doping concentration in BTMO system [26]. Also, the observed decrease in the direct band gap value with doping concentrations increases indicate the red shift in the absorption edge as observed [27]. The enhancement in the redshift with the increase of Mn doping concentration is associated with an increase in crystallite size and a decrease of the energy band gap. The band-gap between the valence band and conduction band are decreased due to a higher possibility of electrons jump from the valence band to conduction band. As a result, we absorbed an increase in conductance which was observed in Mn-doped BTO materials [28].

3.5 Luminescent properties

Photoluminescence (PL) spectroscopy is used to examine the efficiency of trapping, separating, and transferring charge carriers mostly in semiconductors. In ABO_3 structure, particularly the oxygen vacancies are the most dominant defect centers along with contributes to the creation of oxygen vacancy associated with defects and free charge carriers [15].

The PL emission spectra of pure and Mn-doped BTO with an excitation wavelength of 430 nm were shown in Fig. 5. The recombination of electrons and holes in the delocalized states is responsible for the emission in the visible region. These delocalized states are due to the intrinsic structural defects related to the symmetry of the Mn-doped BTO system. In all the samples Mn ions act as an acceptor type dopant and expected to doped at Ti ion site. The incorporation of the Mn ion into the Ti ion lattice leads to the formation of doubly charged oxygen vacancies to compensate the charge imbalance. Moreover, the surface effect of OH-defect and non-symmetric Ti ion site are intrinsic type defect in BTMO samples [11]. The visible PL emission indicates that the more ordered and disordered structure of perovskite (ABO_3) materials through the green, yellow, orange and red emission [29]. In order to understand the nature of PL emission of the pure and Mn-doped BTO ceramic materials, each spectrum was subjected to Gaussian fitting independently and individual peaks were obtained through the de-convolution process and observed results are shown in Table 3 [30, 31]. From Fig. 5, it is clear that there are three strong emission peaks at around 533 nm (green), 595 nm (orange) and 717 nm (red) were observed. Accordingly, the weak emission peaks were also found at 576, 619, 644, 667, 687, 737 nm. The visible green emission band observed at 533 nm is due to the presence of host lattice defects, oxygen vacancies or lattice defects. In particular, the visible region green emission is self-activated phosphor luminescence type which the can be realized

Fig. 4 (a) UV-spectra of a $BaTi_{1-x}Mn_xO_3$ ($x = 0.00, 0.25, 0.50, 0.75$ mol%) samples; (b) energy band gap of a Tauc's plot $BaTi_{1-x}Mn_xO_3$ ($x = 0.00, 0.25, 0.50, 0.75$ mol%) samples

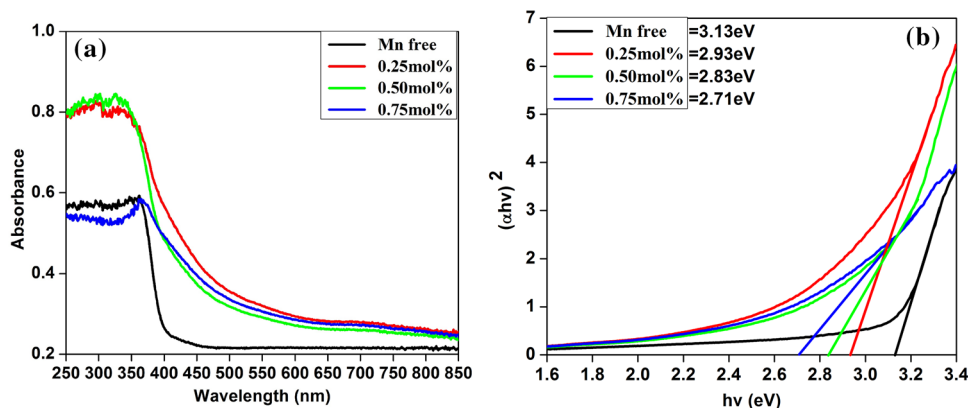
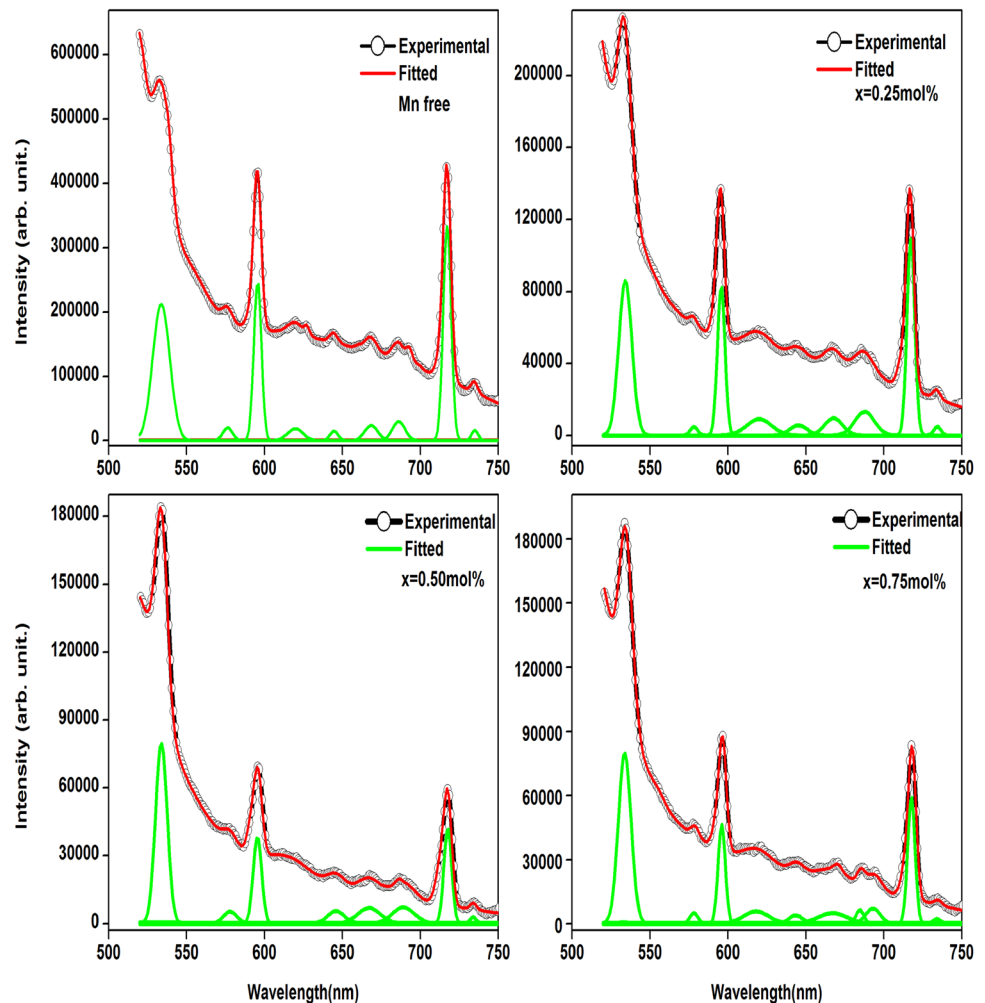


Table 3 PL modes and full width half maxima of a $\text{BaTi}_{1-x}\text{Mn}_x\text{O}_3$ ($x = 0.00, 0.25, 0.50, 0.75$ mol%) samples

PL peaks (nm)				FWHM (nm)			
$x = 0.0\%$	$x = 0.25\%$	$x = 0.50\%$	$x = 0.75\%$	$x = 0.0\%$	$x = 0.25\%$	$x = 0.50\%$	$x = 0.75\%$
533.31	533.83	533.52	533.71	7.66	12.13	9.79	10.30
595.51	595.71	595.39	595.99	6.20	5.98	6.86	5.78
717.22	717.31	717.57	717.63	6.26	6.21	6.08	5.94

Fig. 5 PL emission spectra of ($\text{BaTi}_{1-x}\text{Mn}_x\text{O}_3$) ($x = 0.25, 0.50, 0.75$ mol%) samples for excitation of 435 nm

in perovskite systems [32]. The weak yellow emission at 576 nm is attributed to the trapping in the vicinity of crystal defects and impurities. The two emission peaks centered at 596 nm (orange band) and 717 nm (red band) in the visible region for BTMO ceramics hardly reported earlier. It may be attributed to the synthesis condition as Mn substituted in BTO. We can observe that the intensity of PL emission decreases with increasing Mn concentration, which indicates that decrease in oxygen vacancies and reduction in the number of electrons may be attributed to the Burstein–Moss shift [27].

3.6 Dielectric constant and dielectric loss

The dielectric constant and loss of $\text{BaTi}_{1-x}\text{Mn}_x\text{O}_3$ ($x = 0, 0.25, 0.50, 0.75$ mol%) ceramics for different concentrations have been measured as a function of frequency in the range of 1 Hz to 1 MHz at room temperature, are exposed in Fig. 6a, b respectively. It is observed that the increase in frequency, the value of the dielectric constant decreases to 100 kHz, thereafter it becomes almost constant for all the samples. The value of dielectric constant has been found to 5.53×10^3 , 8.93×10^3 , 1.13×10^4 and 2.61×10^4 for $x = 0,$

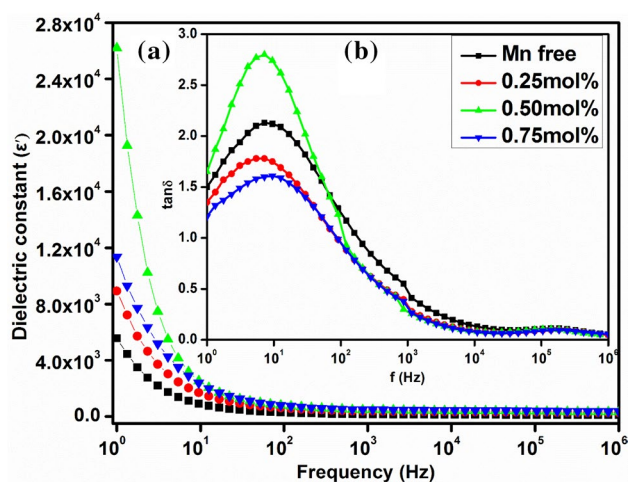


Fig. 6 Room temperature (a) dielectric constant (b) dielectric loss of a $\text{BaTi}_{1-x}\text{Mn}_x\text{O}_3$ ($x=0.00, 0.25, 0.50, 0.75$ mol%) samples

0.25, 0.50, 0.75 mol% at room temperature. The enhancement of dielectric constant in Mn-doped samples is associated with the electronic structure of Mn^{3+} and A-B bond. The hopping of Mn^{2+} to Mn^{3+} results in orientational polarization that may be visualized as an exchange of electrons between these ions. The introduction of Mn may result in the distortion of TiO_6 octahedron, leading to the creation of oxygen vacancies and may also weaken the A-B sub lattice interaction, allowing less resistance to polarization and thus enhance the dielectric constant. During the exchange mechanism, the electron has passed through a grains and grain boundary of the dielectric medium. Owing to the high resistance of the grain boundary, the electrons accumulate at the grain boundary and produce space charge polarization. It is well known that the grain boundaries are more effective at low frequency and grain are effective at high frequency [22]. Hence, due to grain boundary affect the dielectric constant decreases rapidly in the low-frequency region, At high frequency, the grain comes into action and also the hopping of electrons cannot follow the high-frequency ac field. Figure 6 also depicts that dielectric constant increase with the increase of Mn doping, which also affected by factors such as grain size, density, and porosity of the samples.

The dielectric loss factor $\tan \delta$ (ϵ''/ϵ') measures the energy loss within the samples. The dielectric loss arises when the polarization lags behind the applied ac field and is also caused by an imperfection in the crystal lattice. It is found that the value of $\tan \delta$ has very high in the low-frequency region. A hump is seen around lower frequency and is suppressed at a high frequency that may be due to the possibility of space charge relaxation. The orientational polarization is the dominant mechanism above 100 Hz and increases below 100 Hz is due to the electrode polarization of both dielectric constant and loss. The BMTO exhibit space charge

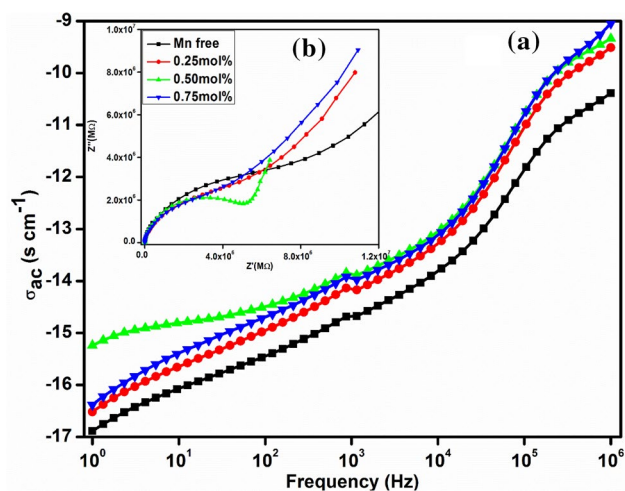


Fig. 7 Room temperature (a) ac conductivity (b) impedance of a $\text{BaTi}_{1-x}\text{Mn}_x\text{O}_3$ ($x=0.00, 0.25, 0.50, 0.75$ mol%) samples

polarization due to their structural in-homogeneities, which are confirmed by EPR and PL spectra. The ceramic materials contain a number of surface defects, such as oxygen and Ba/Ti vacancies and porosity at the grain boundaries due to their large surface-to-volume ratio in perovskite BMTO [12, 32].

3.7 AC conductivity analysis

Figure 7a shows a variation of ac conductivity (σ_{ac}) as a function of frequency in the range 1 Hz–1 MHz at room temperature. The value of σ_{ac} is calculated using the formula.

$$\sigma_{ac} = \epsilon_0 \epsilon' \omega \tan \delta \quad (3)$$

where ϵ_0 is the permittivity of free space, ϵ' is the relative permittivity, ω is the angular frequency and $\tan \delta$ is the dielectric loss. It is observed that σ_{ac} increasing trend with an increase in frequency. This is due to fact that BTO is a good ferroelectric material, generally, these materials are a good insulator with the absence of unpaired electrons. The doping of Mn ions on B-site with d^n configuration increase the dielectric constant value is expected and hence leading to an increase in conductivity of the system with an increased number of charge carriers. In the present system, conductivity amplifies due to increasing of Mn concentration of charge carriers like oxygen vacancies which arise by intrinsic or extrinsic processes [12]. The oxygen vacancies may arise due to the Mn doping concentration to charge neutrality of ceramics and this fact is also supported by EPR studies. The charge neutrality to maintain the oxygen vacancies of the lower valence of a $\text{Mn}^{2+}/\text{Mn}^{3+}$ ion at B site, replacing $\text{Ti}^{4+}/\text{Ti}^{3+}$ ceramics. At lower frequencies, the grain boundaries are more active and hence the hopping of $\text{Mn}^{2+}/\text{Mn}^{3+}$ ions is less at lower frequencies. As the frequency of applied field increases, the conductive grains become more active

thereby promoting the hopping between $\text{Mn}^{2+}/\text{Mn}^{3+}$ ions, thereby increasing the hopping conduction [33]. Therefore, an increase in Mn ion concentration leads to an enhancement in conductivity.

3.8 Impedance analysis

Impedance spectroscopy is ideal for investigating the electrical response of dielectric materials as a function of frequency. It is a powerful technique for unraveling the complexities of materials, whose properties and application depends upon the close control of structure, composition and dopant atoms, which functions by utilizing the different frequency dependences of constituent components for their separation. The imaginary parts of impedance (Z'') versus real part of impedance (Z') (Nyquist plots) for $\text{BaTi}_{1-x}\text{Mn}_x\text{O}_3$ (where $x = 0, 0.25, 0.50, 0.75$ mol%) has been plotted over wide frequency at room temperature, shown in Fig. 7b.

It has been observed that in general there exist two semicircles at higher frequency region is attributed to the grain property of the material, whereas, at the low-frequency region is attributed to the grain boundary properties. In the present investigation, flat single semicircle was observed for each sample between the frequencies ranges 1 Hz to 1 MHz. The diffusion of charge transport is more dominant in the low-frequency region. The diameter of the semicircle decreases with increasing Mn dopant, referring to the pronounced increase of conductivity. This lower resistance with increasing Mn dopant promotes the rate of electron hopping, which is the sole process for both conduction and polarization in the samples [25, 34].

3.9 Ferroelectric properties

The room temperature ferroelectric hysteresis (P–E) loops for $\text{BaTi}_{1-x}\text{Mn}_x\text{O}_3$ ($x = 0.00, 0.25, 0.50, 0.75$ mol%) ceramics were recorded at a constant frequency (20 Hz) and at different applied voltage measurements (50 kV, 60 kV and 70 kV) are shown in Fig. 8. The pristine BTO ceramic shows an extensive loop for the applied voltages, it is observed that even for such a high electric field, the P–E loop could not be fully saturated [18]. However, in the case of Mn-doped BTO samples, a double well-saturated hysteresis loop with a decrease in the coercive electric field (E_c) and remanent polarization (P_r) has been observed. It is found that the hysteresis loops change expressively with grain size. The grain size dependence of the remanent polarization (P_r) and coercive electric field (E_c). The lower P_s and the higher E_c values for BTO may arise frozen polarization induced by pinning centers as due to a large number of grain boundaries and charged defects due to smaller grain size [35]. The observed unsaturated polarization for BTO can be clarified by the contribution of three noteworthy effects:

(i) the reduction of the tetragonal strain (ii) reduction of the local effective field owing the presence of low-permittivity grain boundaries (iii) pinning of the irreversible domain wall movement by grain boundaries and/or charged defects isolated at the grain boundaries [36].

This double P–E loop was usually observed in ferroelectric (FE) and antiferroelectric (AFE) nature of ceramic materials, which was due to the presence of defects and anti-parallel dipoles in the samples [37]. In the present case, for pure and Mn-doped BTO samples show characteristic ferroelectric hysteresis loops with maximum polarization (P_{Max}), remnant polarization (P_r) and coercive fields (E_c) and the observed results are summarized in Table 4. It was clear from Table 4 with an increase in Mn doping concentration, a finite decrease in P_r and E_c was observed. This reduction in P_r values indicates that the higher profusion of the AFE state has reasonably decreased the volume of FE state. The increase of Mn concentration in the BTO lattice also leads to the decrease of FE order and enhances the AFE order at room temperature for BTMO samples [38].

In other words, both the FE and AFE order can coexist in the BTMO system, which confirms that the FE order tends to disappear and AFE order tends to appear as Mn concentration increases [39]. The ionic radius of Ti (0.68 Å) is lower than that of Mn (0.46 Å) causes interatomic between the off-center TiO_6 dipoles and have a leakage behavior of Mn-doped BTO samples. This difference in ionic radius can also cause doping distortion of oxygen octahedron, which decreases the long-range order of FE domains and the stability of FE domains. This reduction may be ascribed due to the transformation of FE to AFE state in Mn-doped BTO samples [40]. In addition to the above, the depolarizing field arises from the presence of low permittivity nature at the ferroelectric grain boundary layer which remains shown a strong depression of ferroelectric properties as observed from the slim P–E loops. In the present case, we observed for BTO polycrystalline materials are expected to have weak ferroelectric properties with very small grain size (< 50 nm) for $x = 0.00, 0.25\%$ Mn-doped BTO ceramics. This was due to a combined effect of a simple domain structure, which cannot readily deform under by external electric field and the pinning of domain wall with the suppression of large-scale domain switching and the presence of defects segregated at the grain boundary [40].

3.10 EPR spectral analysis

The electron paramagnetic resonance (EPR) is an influential tool for identifying the several paramagnetic point and vacancy defects in a compound. In the present work, for ABO_3 perovskite systems, such as ionized Ba and Ti vacancies in BTO lattice were identified through EPR measurements. The EPR spectra of pure and Mn-doped BTO were

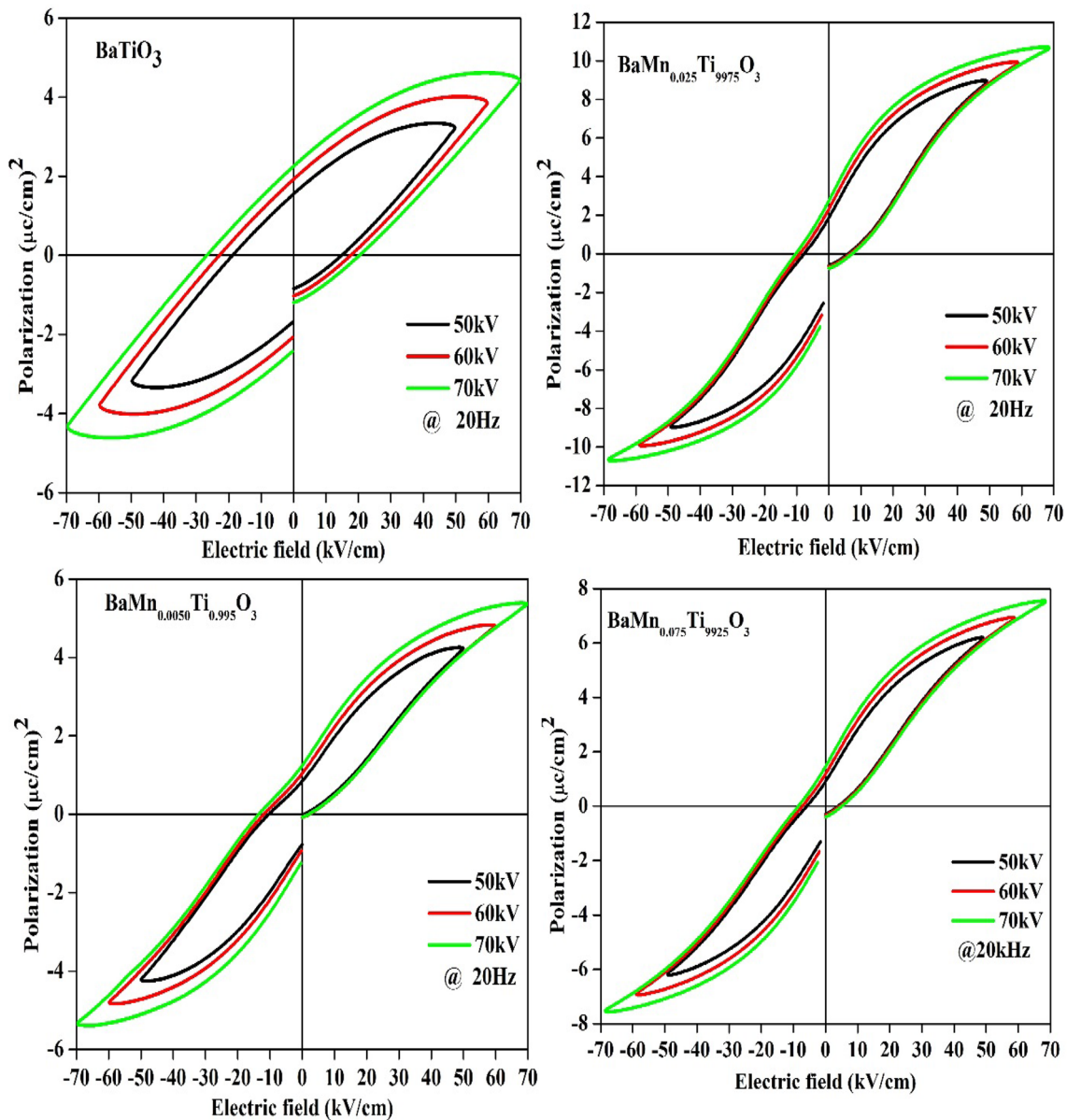


Fig. 8 Room temperature P–E loops of a $\text{BaTi}_{1-x}\text{Mn}_x\text{O}_3$ ($x = 0.00, 0.25, 0.50, 0.75$ mol%) samples measured at 20 Hz frequency and at different voltages

shown in Fig. 9. At room temperature. The gyromagnetic (g) ratio value was calculated using,

$$h\nu_0 = g\beta H \quad (4)$$

where h is the Planck's constant, ν_0 is the microwave frequency, β is the Bohr magneton H is the applied magnetic field strength.

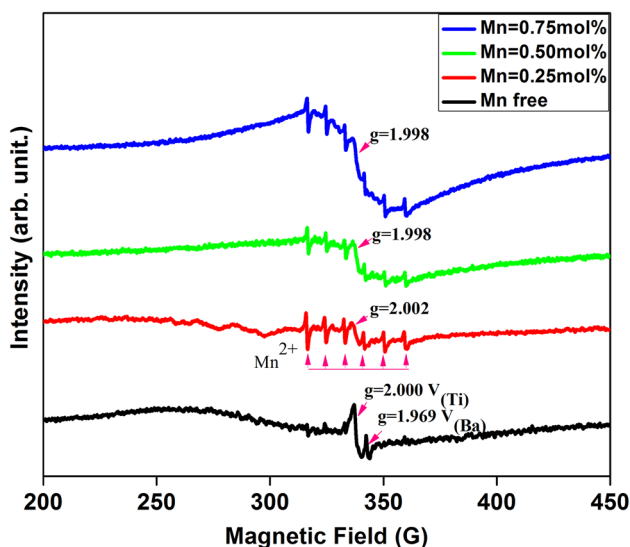
The EPR signal for BTO sample revealed two paramagnetic singlets with variable intensity at $g = 1.969$ singlet to barium vacancies (V_{Ba}) and $g = 2.000$ singlets can be tentatively assigned to ionized Ti-vacancy defects (V_{Ti}) [16]. A weak singlet signal with $g = 1.969$ was associated with

intrinsic point defects which may be present in undoped BTO. Figure 9 shows an increase in the intensity with increasing Mn dopant in BTO lattice with a decrement in the g factor. The six resonance sharp peaks are due to the hyperfine splitting of the Mn isotope nuclear spin of $5/2$ [41]. The EPR signals from Mn^{2+} depends on dopant site preference, the dopant content, and particle size also on the Ba/Ti ratio. In the literature, the formation of V_{Ba} and V_{Ti} signals in EPR spectra of ceramics correlates with the appearance of the positive temperature coefficient of resistivity (PTCR) effect [41]. The spectra of Mn-doped BTO shows a strong EPR signal at $g = 2.000$ to 1.998 appeared

Table 4 Room temperature P–E loops of a $\text{BaTi}_{1-x}\text{Mn}_x\text{O}_3$ ($x=0.00, 0.25, 0.50, 0.75$ mol%) samples

Composition	Field (kV/cm)	P_{Max} ($\mu\text{C}/\text{cm}^2$)	P_r ($\mu\text{C}/\text{cm}^2$)	E_c (kV/cm)
BaTiO_3	50	3.234	1.573	14.572
	60	3.863	1.970	17.264
	70	4.391	2.283	19.620
$\text{Ba Mn}_{0.0025}\text{Ti}_{0.9975}\text{O}_3$	50	8.994	1.887	5.962
	60	9.909	2.291	6.608
	70	10.683	2.780	7.151
$\text{Ba Mn}_{0.0050}\text{Ti}_{0.995}\text{O}_3$	50	4.278	0.865	0.575
	60	4.795	1.061	1.994
	70	5.370	1.245	2.173
$\text{BaMn}_{0.0075}\text{Ti}_{0.9925}\text{O}_3$	50	6.196	0.901	3.929
	60	6.917	1.173	4.404
	70	7.536	1.469	5.055

for different concentrations at 0.25 to 0.75 mol% and it explores that the B-site occupation of Mn^{2+} at Ti^{4+} site. Since, the Mn as an acceptor dopant, at 0.25 mol% concentrations of Mn in BTO lattice, shows a good correlation with a defect compensation mechanism of acceptor-doped BTO ceramics. In order to find out geometric signal variable intensity at $g=2.000, 2.002, 1.998$ and 1.998 in samples with Mn addition as well resolved sextet signals which are caused by Mn^{2+} in BTO ceramics [42]. These signals are related to cation vacancies for different Mn^{2+} ion concentrations. This concludes that paramagnetic ion Mn^{2+} is very sensitive to the symmetry changes which occur at the Ti site for all the structural transition.

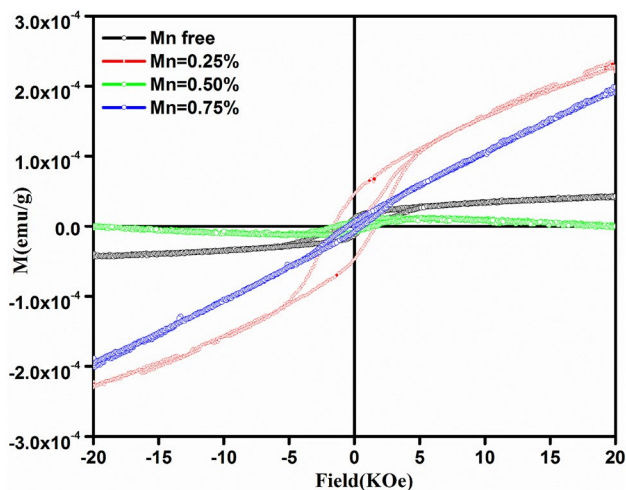
**Fig. 9** EPR spectrum of a $\text{BaTi}_{1-x}\text{Mn}_x\text{O}_3$ ($x=0.00, 0.25, 0.50, 0.75$ mol%) samples

3.11 Room temperature magnetic properties

The magnetization curves for BTMO ceramics measured at room temperature is depicted in Fig. 10. For a pristine sample, magnetic hysteresis loops exhibit weak ferromagnetic (WFM) behavior. From Fig. 10, the dopant ion concentration (Mn) in Ti-site increases as $x=0.25, 0.50, 0.75$ mol% in BTO lattice, a finite change in the shape of the hysteresis loops were observed, which proves the concentration (induced free carrier) dependent on the observed ferromagnetism. In the present case, the free charge carriers are produced due to the difference in the valence of Ti^{3+} and $\text{Mn}^{2+}/\text{Mn}^{3+}$ [9, 12, 13]. Also, the magnetization value initially increases then decreases (2.3449 to 1.9866×10^{-4} emu/g) with the increase of doping concentration, which indicating the coexistence of ferromagnetism (FM) and antiferromagnetic (AFM) and also system has increased surface area due to the decrement in particle sizes. This reduction in particle size upon doping is attributed to the difference in ionic radius between Ti and Mn. It is known that the ionic radii of Ti^{4+} and Ti^{3+} are 0.605 \AA and 0.67 \AA respectively, and ion radii of Mn^{2+} (low spin/high spin) and Mn^{4+} are $0.58 \text{ \AA}/0.65 \text{ \AA}$ and 0.54 \AA [12, 14]. The magnetism for pristine is likely to be related to intrinsic defects of oxygen vacancies and oxygen vacancies mediated coupling of Ti ions. For 0.25% Mn-doped BTO samples, an enhancement of ferromagnetic behavior was observed. However, the sample at 0.50% Mn in the BTO sample shows the competition between FM and AFM. This mixed behavior may be due to the combined effect of oxygen vacancies as well as the external magnetic field [32]. For $x=0.75\%$ Mn doped BTO sample demonstrates obviously the surface ferromagnetic behavior. The M_s , M_r and H_c also decrease upon Mn substitution as reported in Table 5. Meanwhile, at a lower concentration, dopant atom Mn exactly replaces Ti^{3+} . On increasing the dopant concentration ($x=0.50, 0.75$ mol%) the dopant atoms may get segregated at the grain boundary.

Table 5 Calculated parameter from room temperature magnetic hysteresis loop on $\text{BaTi}_{1-x}\text{Mn}_x\text{O}_3$ ($x=0.00, 0.25, 0.50, 0.75$ mol%) samples

Composition	M_s (emu/g)	M_r (emu/g)	H_C (Oe)	EB (Oe)	Grain size (nm)
BaTiO_3	4.2968×10^{-5}	1.1802×10^{-5}	895	76.15	41
$\text{Ba Mn}_{0.0025}\text{Ti}_{0.9975}\text{O}_3$	2.3449×10^{-4}	4.6688×10^{-5}	1662	28.33	51
$\text{Ba Mn}_{0.0050}\text{Ti}_{0.995}\text{O}_3$	1.2411×10^{-5}	7.4734×10^{-6}	1497	42.43	53
$\text{BaMn}_{0.0075}\text{Ti}_{0.9925}\text{O}_3$	1.9866×10^{-4}	6.6954×10^{-6}	602	41.13	63

**Fig. 10** Room temperature magnetic hysteresis loop on $\text{BaTi}_{1-x}\text{Mn}_x\text{O}_3$ ($x=0.00, 0.25, 0.50, 0.75$ mol%) samples

The charge imbalance, the ferromagnetic oxygen vacancies mediated coupling could be collapsed by paramagnetic Mn ions incorporated randomly into BTO lattices [14] and contribute to the peculiar M-H loop observed for ($x=0.50, 0.75$ mol%). The unsaturated FM loop in the M-H curve as shown in Fig. 10. For $x=0.50\%$ proves the coexistence of FM and AFM phases. In this present case, the ferromagnetic interactions become more dominant. Hence, it is evident that Mn^{2+} and Mn^{3+} ions exist in our sample. The result is also evident by the superposition of those signals, from the EPR analysis. Among these, that exchange interactions between the defect induced carriers and $\text{Mn}^{2+}/\text{Mn}^{3+}$ magnetic ions are responsible for FM, while other exchange interactions are antiferromagnetic.

4 Conclusion

In summary, the multifunctional behavior of Mn-doped BTO ceramics was successfully synthesized by sol-gel combustion method. The crystallographic tetragonal phase is confirmed by XRD and Raman. Further, an increase in lattice parameters, crystallite sizes, and unit cell volumes due to the substitution of smaller ionic radius of Mn^{2+} ion in Ti site

ions. Raman spectra independently confirm the tetragonal symmetries through the presence of a band at 306 cm^{-1} . The optical band gap decrease from 3.13 to 2.71 eV indicates the presence of a red shift due to increasing Mn doping in BTO samples. PL reveals an intense emission peak at 533 nm (green), 595 nm (orange), and 717 nm (red) in the visible region from 550 to 800 nm. On increasing the Mn ion concentration decrease in PL intensity is observed due to the increased structural order and the decrease in the oxygen vacancy defects. Dielectric constant and ac conductivity are improved with Mn doping. The appearance of P-E double hysteresis loop confirms the ferroelectric properties of the material. The EPR results indicate that signals at $g=1.969$ and 2.000 assigned for ionized Ba and Ti-vacancy defects. The M-H analysis indicates the change of WFM-FM, because of the exchange interactions between the defects induced carriers and $\text{Mn}^{2+}/\text{Mn}^{3+}$ magnetic ions. Therefore, enhancement in the dielectric constant value and magnetic phase transition associated with the migration of oxygen vacancies and carrier hopping process between Mn^{2+} and Mn^{3+} ions.

Acknowledgements The authors thankful to Department of Physics, NIT Tiruchirappalli for the multiferroic tester facility (MHRD, Government of India) for PE measurements.

References

1. C. Srilakshmi, R. Gowravaram, R. Saraf, The effect of nature of transition metal dopant in BaTiO_3 perovskite on catalytic reduction of nitrobenzene. *RSC Adv* **5**, 45965–45973 (2015)
2. S. Nayak, B. Sahoo, K. Chaki, D. Khastgir, Facile preparation of uniform barium titanate (BaTiO_3) multipods with high permittivity: its Impedance and temperature dependent dielectric. *RSC Adv* **4**, 1212–1224 (2014)
3. H. Gong, X. Wang, S. Zhang, Z. Tian, L. Li, H. Gong, X. Wang, S. Zhang, Z. Tian, L. Li, Electrical and reliability characteristics of Mn-doped nano BaTiO_3 -based ceramics for ultrathin multilayer ceramic capacitor application. *J. Appl. Phys.* **112**, 114119 (2014)
4. S. Yoon, J. Park, C. Kim, D. Kim, S. Yoon, J. Park, C. Kim, D. Kim, Difference between compositional and grain size effect on the dielectric nonlinearity of Mn and V-doped BaTiO_3 multilayer ceramic capacitors. *J. Appl. Phys.* **115**, 244101 (2014)
5. K.C. Verma, R.K. Kotnala, Multiferroic approach for Cr, Mn, Fe, Co, Ni, Cu substituted BaTiO_3 nanoparticles. *Mater. Res. Express* **3**, 055006 (2016)

6. X. Zhao, W. Chen, L. Zhang, L. Zhong, The effect of the bipolar field on the aging behavior and the associated properties of the Mn-doped BaTiO₃ ceramics. *J. Alloys Compd.* **618**, 707–711 (2015)
7. W. Chen, X. Zhao, J. Sun, L. Zhang, L. Zhong, Effect of the Mn doping concentration on the dielectric and ferroelectric properties of different-routes-fabricated BaTiO₃-based ceramics. *J. Alloys Compd.* **670**, 48–54 (2016)
8. Y.Y. Guo, Y. Zhao, H.G. Zhang, N. Zhang, Ceramics during ferroelectric-ferroelectric transition cycle. *J. Alloys Compd.* **696**, 814–819 (2017)
9. N.V. Dang, T. Phan, T.D. Thanh, V.D. Lam, L.V. Hong, Structural phase separation and optical and magnetic properties of BaTi_{1-x}Mn_xO₃ multiferroics. *J. Appl. Phys.* **111**, 113913 (2012)
10. X. Zhao, W. Chen, L. Zhang, Effect of fabrication routes on the microstructure, the dielectric and ferroelectric properties of the Mn-doped BaTiO₃ ceramics. *Appl. Phys. A.* **118**, 931–938 (2015)
11. M.K. Rath, Characterization and photoluminescence studies on hydrothermally synthesized Mn-doped barium titanate nano powders. *Mater. Lett.* **61**, 4821–4823 (2007)
12. A. Rani, A. Rani, J. Kolte, P. Gopalan, Phase formation, microstructure, electrical and magnetic properties of Mn substituted barium titanate Phase formation, microstructure, electrical and magnetic properties. *Ceram. Int.* **41**, 14057–14063 (2015)
13. T. Phan, P. Zhang, D. Grinting, S.C. Yu, N.X. Nghia, Influences of annealing temperature on structural characterization and magnetic properties of Mn-doped BaTiO₃ ceramics. *J. Appl. Phys.* **112**, 013909 (2012)
14. Y. Shuai, S. Zhou, D. Bürger, H. Reuther, I. Skorupa, Decisive role of oxygen vacancy in ferroelectric versus ferromagnetic Mn-doped BaTiO₃ thin films. *J. Appl. Phys.* **109**, 084105 (2011)
15. I.J. Berlin, B. Nair, G.P. Daniel, P.V. Thomas, Influence of annealing temperature and oxygen atmosphere on the optical and photoluminescence properties of BaTiO₃. *J. Mater. Sci.* **24**, 848–854 (2013)
16. D. Lu, L. Yuan, W. Liang, Z. Zhu, Characterization of oxygen vacancy defects in Ba_{1-x}Ca_xTiO₃ insulating ceramics using electron paramagnetic resonance technique. *Jpn. J. Appl. Phys.* **55**, 011501 (2016)
17. Y.Y. Guo, J. Liu, Y.F. Guo, T. Wei, Y.J. Guo, N. Zhang, Y.Y. Guo, J. Liu, Y.F. Guo, T. Wei, Y.J. Guo, N. Zhang, External field effects on aging phenomenon of acceptor-doped BaTiO₃ ceramics. *AIP Adv.* **5**, 97107 (2015)
18. E. Venkata Ramana, F. Figueiras, A. Mahajan, D.M. Tobaldi, B.F.O. Costa, M.P.F. Graça, M.A. Valente, Effect of Fe-doping on the structure and magnetoelectric properties of (Ba_{0.85}Ca_{0.15})(Ti_{0.9}Zr_{0.1})O₃ synthesized by a chemical route. *J. Mater. Chem. C.* **4**, 1066–1079 (2016)
19. R. Roukos, N. Zaiter, D. Chaumont, Relaxor behaviour and phase transition of perovskite. *J. Adv. Ceram.* **7**, 124–142 (2018)
20. P. Xue, Y. Hu, W. Xia, H. Wu, X. Zhu, Molten-salt synthesis of BaTiO₃ powders and their atomic-scale structural characterization. *J. Alloys Compd.* **695**, 2870–2877 (2017)
21. H. Ávila, L. a Ramajo, M.S. Góes, M.M. Reborado, M.S. Castro, R. Parra, Dielectric behavior of epoxy/BaTiO₃ composites using nanostructured ceramic fibers obtained by electrospinning. *ACS Appl. Mater. Interfaces* **5**, 505–510 (2013)
22. H.A. Ávila, L.A. Ramajo, M.M. Reborado, M.S. Castro, R. Parra, Hydrothermal synthesis of BaTiO₃ from different Ti-precursors and microstructural and electrical properties of sintered samples with submicrometric grain size. *Ceram. Int.* **37**, 2383–2390 (2011)
23. H.A. Ávila, M.M. Reborado, R. Parra, M.S. Castro, Dielectric permittivity calculation of composites based on electrospun barium titanate fibers. *Mater. Res. Express.* **2**, 45302 (2015)
24. C. Gao, Q. Fu, D. Zhou, H. Zu, T. Chen, F. Xue, Nanocrystalline semiconducting donor-doped BaTiO₃ ceramics for laminated PTC thermistor. *J. Eur. Ceram. Soc.* **37**, 1523–1528 (2017)
25. P.M.M. Gazzali, G. Chandrasekaran, Electrical and magnetic phase transition studies of Fe and Mn co-doped BaTiO₃. *J. Alloys Compd.* **656**, 98–109 (2015)
26. N. Rajamanickam, K. Jayakumar, K. Ramachandran, Influence of Mn ion on flower shaped perovskite BaTiO₃ nanostructures based dye-sensitized solar cell. *Nano-Struct. Nano-Objects.* **9**, 19–25 (2017)
27. S. Samant, M. Muralidhar, V. Sankaranarayanan, K. Sethupathi, M.S. Ramachandra Ra, M. Murakami, Band gap reduction and red-shift of lattice vibrational spectra in Nb and Fe co-doped PLZT. *J. Mater. Sci.* **52**, 13012–13022 (2017)
28. Y. Qi, L. Zhang, G. Jin, Y. Wan, Y. Tang, D. Xu, Q. He, F. Wang, Y. Li, D. Sun, UV-visible spectra and conductive property of Mn-doped BaTiO₃ and Ba_{0.93}Sr_{0.07}TiO₃ ceramics. *Ferroelectrics.* **458**, 64–69 (2014)
29. L.V. Maneeshya, P.V. Thomas, K. Joy, Effects of site substitutions and concentration on the structural, optical and visible photoluminescence properties of Er doped BaTiO₃ thin films prepared by RF magnetron sputtering. *Opt. Mater. (Amst.)* **46**, 304–309 (2015)
30. S.K. Ghosh, S.K. Rout, Induced instability in local structure and ferroelectric polarization of rare earth modified BZT relaxor ceramics. *Curr. Appl. Phys.* **16**, 989–1000 (2016)
31. E. Devi, B.J. Kalaiselvi, K. Madhan, D. Vanidha, S.S. Meena, R. Kannan, Quantification of charge carriers participating antiferromagnetic to weak ferromagnetic phase transition in Na doped LaFeO₃ nano multiferroics. *J. Appl. Phys.* **124**, 8 (2018)
32. N. Sharma, A. Gaur, U. Kr, Multiferroic behavior of nanocrystalline BaTiO₃ sintered at different temperatures. *Ceram. Int.* **40**, 16441–16448 (2014)
33. M. Kanta, N. Sangwan, S. Ahlawat, S. Rani, R.S. Rani, Kundu, Influence of Mn doping on electrical conductivity of lead free BaZrTiO₃ perovskite ceramic. *Ceram. Int.* **44**, 10315–10321 (2018)
34. K.M. Batoo, S. Kumar, C.G. Lee, Alimuddin, Study of dielectric and ac impedance properties of Ti doped Mn ferrites. *Curr. Appl. Phys.* **9**, 1397–1406 (2009)
35. V.R. Mudinepalli, L. Feng, W.-C. Lin, B.S. Murty, Effect of grain size on dielectric and ferroelectric properties of nanostructured Ba_{0.8}Sr_{0.2}TiO₃ ceramics. *J. Adv. Ceram.* **4**(1), 46–53 (2015)
36. L. Curecheriu, S.-B. Balmus, M.T. Buscaglia, V. Buscaglia, A. Ianculescu, L. Mitoseriu, Grain size-dependent properties of dense nanocrystalline barium titanate ceramics, *J. Am. Ceram. Soc.* **95**, 1–10 (2012)
37. T. Zhang, W. Li, Y. Hou, Y. Yu, W. Cao, Y. Feng, W. Fei, Positive/negative electrocaloric effect induced by defect dipoles in PZT ferroelectric bilayer thin films. *RSC Adv.* **6**, 71934–71939 (2016)
38. M. Chandrasekhar, P. Sonia, Kumar, Synthesis and characterizations of NaNbO₃ modified BNT-BT-BKT ceramics for energy storage applications. *Phys. B Condens. Matter.* **497**, 59–66 (2016)
39. S.K. Das, B.K. Roul, Double hysteresis loop in BaTi_{1-x}Hf_xO₃ ferroelectric ceramics. *J. Mater. Sci. Mater. Electron.* **26**, 5833–5838 (2015)
40. M.T. Buscaglia, M. Viviani, V. Buscaglia, L. Mitoseriu, A. Testino, P. Nanni, Z. Zhao, M. Nygren, C. Harnagea, D. Piazza, C. Galassi, High dielectric constant and frozen macroscopic polarization in dense nanocrystalline BaTi O3 ceramics. *Phys. Rev. B* **73**, 1–10 (2006)
41. T. Kolodiaznyhi, A. Petric, Analysis of point defects in polycrystalline BaTiO₃ by electron paramagnetic resonance. *Phys. Chem. Solids* **64**, 953–960 (2003)
42. D. Lu, X. Sun, B. Liu, J. Zhang, T. Ogata, Structural and dielectric properties, electron paramagnetic resonance, and defect chemistry of Pr-doped BaTiO₃ ceramics. *J. Alloys Compd.* **615**, 25–34 (2014)